# Characterization of debonding strength in steel-wire-reinforced aluminum and its influence on material fracture

**A. Morasch, A. Reeb, H. Baier, Kay A. Weidenmann, V. Schulze**

**Angaben zur Veröffentlichung / Publication details:**

Morasch, A., A. Reeb, H. Baier, Kay A. Weidenmann, and V. Schulze. 2015. "Characterization of debonding strength in steel-wire-reinforced aluminum and its influence on material fracture." *Engineering Fracture Mechanics* 141: 242–59. https://doi.org/10.1016/j.engfracmech.2015.05.029.

# Characterization of debonding strength in steel-wire-reinforced aluminum and its influence on material fracture

A. Morasch [a,*], A. Reeb [b], H. Baier [a], K.A. Weidenmann [b], V. Schulze [b]

[a] *Institute of Lighweight Structures, TU München, Germany*
[b] *Institute of Applied Materials, Karlsruhe Institute of Technology, Germany*

## 1. Introduction

The research of the collaborative research center CRC Transregio10 covers the issue of material processing for composite extrusion and the resulting mechanical properties of steel-wire-reinforced aluminum extrusions. A scheme of the composite extrusion process is shown in Fig. 1 and an extruded reinforced section of steel-wire-reinforced aluminum extrusions can be seen in Fig. 2. Previous investigations focused on interface properties, mechanical properties as well as the deformation and damage behavior in quasi-static and cyclic testing of aluminum and magnesium alloys reinforced with steel wires.

Essential work on material selection, resulting interface properties and mechanical properties with focus on an EN AW-6060 matrix was performed by [1–3]. It was shown that the interface shear strength strongly depends on surface treatment of the reinforcing element and the material combination [1,3]. The range of the interface shear strength in a matrix of aluminum EN AW-6060 paired with high strength steel wires of SS301 (1.4310) ranges from 61 MPa (without surface treatment) up to 94 MPa (etched). As the interface shows a good bonding for all variations, a costly surface treatment of the steel wire was foregone. Reinforcing the aluminum matrix EN AW-6060, an increase in stiffness and absolute strength according to the theoretical model of Kelly [4,5] is reached. However, thermal residual stresses arising in the extrusion process lead to a lower elastic limit of the composite [2,6]. Releasing the residual stresses by stretch-forming is thus advisable. Deformation and damage behavior for an elongation in wire direction is characterized by multiple necking of the wire in the composite [7]. This leads to a higher strain to fracture of the wire and an extended fracture strain of the composite.

Further benefits from a steel wire reinforcement in cyclic testing were attested in [1–3,9]. According to [10,11], the fatigue endurance limit can be increased for EN AW-6060 and EN AW-6082 composites. The crack propagation behavior shows

* Corresponding author. Tel.: +49 89 289 16097; fax: +49 89 298 16104.
*E-mail address:* morasch@llb.mw.tum.de (A. Morasch).

**Nomenclature**

| | |
|---|---|
| $A_0$ | initial cross section |
| $A_f$ | minimal cross section after fracture |
| CRC | collaborative research center |
| $E$ | Young's modulus |
| $E_N$ | normal stiffness of cohesive element |
| $E_T$ | tangential stiffness of cohesive element |
| $f$ | present void volume fraction |
| $f*$ | effective void volume fraction |
| $\dot{f}$ | rate of the void volume fraction |
| $f_0$ | initial void volume fraction |
| $f_C$ | critical void volume fraction |
| $f_F$ | fracture void volume fraction |
| $\dot{f}_G$ | growth of existing voids |
| $f_N$ | volume fraction of nucleating particles |
| $\dot{f}_N$ | nucleation of new voids |
| $F_N$ | normal forces acting on interface |
| $F_T$ | shear forces acting on interface |
| GOM | Gesellschaft für optische Messtechnik |
| $k_\omega$ | fitting parameter in Nahshon–Hutchinson model |
| $l_c$ | characteristic element length |
| $N$ | strain hardening parameter of Hockett–Sherby function |
| $p$ | strain hardening parameter of Hockett–Sherby function |
| $q_1, q_2$ | constitutive parameters for Gurson yield function |
| $R_{p0.2}$ | Yield strength at 0.2% plastic strain |
| $R_m$ | Tensile strength at maximum force |
| $S_N$ | standard deviation of mean strain for nucleation |
| SWRA | steel-wire-reinforced aluminum |
| $T$ | temperature |
| $v$ | velocity |
| $\delta_1$ | limit value for constrained fitting approach |
| $\delta_2$ | limit value for constrained fitting approach |
| $\varepsilon$ | true strain |
| $\varepsilon_0$ | prestrain in Voce strain hardening function |
| $\dot{\varepsilon}^p_{eq}$ | rate of plastic equivalent strain |
| $\varepsilon_f$ | fracture strain |
| $\dot{\varepsilon}^p_{kk}$ | rate of plastic volume change |
| $\varepsilon_N$ | mean strain for nucleation |
| $\varepsilon_u$ | ultimate strain |
| $\nu$ | Poisson's ratio |
| $\Phi$ | Gurson yield function |
| $\sigma$ | true stress |
| $\sigma_{eq}$ | equivalent stress for Gurson yield function |
| $\sigma^{\exp}$ | experimental stress |
| $\sigma^{fit}$ | stress given by strain hardening fit |
| $\sigma_{Hyd}$ | hydrostatic stress |
| $\sigma_n$ | normal stress in cohesive element |
| $\sigma_{n,\max}$ | normal strength of cohesive interface |
| $\sigma_s$ | saturation stress – strain hardening function parameter |
| $\sigma_Y$ | yield stress |
| $\tau_{hoop}$ | hoop shear stress |
| $\tau_{\max}$ | shear strength of cohesive interface |
| $\omega(\sigma)$ | function for distinguishing shear stress states |

beneficial phenomena like crack deflection and interface debonding which leads to smaller crack growth rates [2,11]. These contributions show the significance of the interface in such an unidirectionally reinforced composite in different loading and environmental conditions.

The present research shall take advantage of the wide range of previous investigations and add further results for interface assessment for multiple loading conditions. All investigations are performed using steel-wire-reinforced aluminum with the age hardenable aluminum alloy EN AW-6060 as matrix material, which is reinforced with high-strength steel wires with

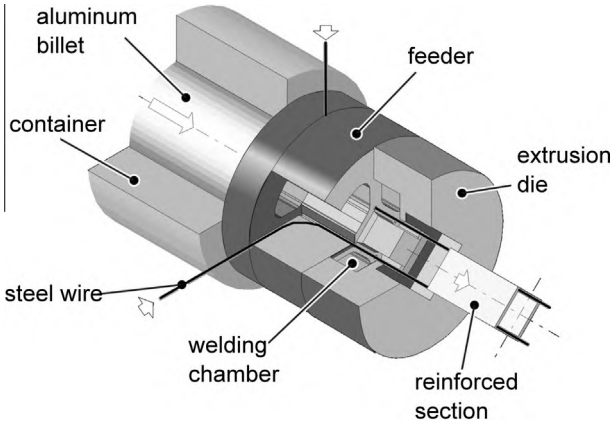


**Fig. 1.** Composite extrusion process (adapted from [8]).

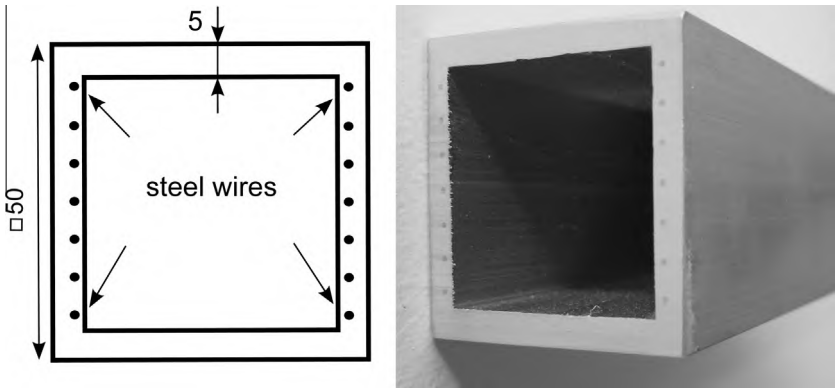


**Fig. 2.** Reinforced extruded section as wrought material for material characterization and analysis.

a diameter of 1 mm, made of SS 301. After assessing the debonding strengths, the influence of the interface normal strength on the mechanical properties of steel-wire-reinforced aluminum is investigated. For that purpose, material properties of steel wire and aluminum matrix are experimentally characterized in Section 2 and material models for simulation are calibrated. Further, a model of the interface between steel wire and aluminum is discussed in Section 3, which includes a description of failure and post-failure friction behavior. The failure model is calibrated based on experimental data from interface-tensile tests and push-out tests.

Taking material fracture into account, a shear modified Gurson model [12] for the aluminum matrix is calibrated and a maximum strain criterion for fracture is used for the steel wires. With simulation models of steel-wire-reinforced aluminum, the materiaĺs sensitivity toward interface strength is assessed in Section 4 for the following two distinct load cases.

- Tension in wire direction
- Tension perpendicular to wire direction.

A comparison of the fracture behavior of steel-wire-reinforced aluminum to non-reinforced aluminum is further carried out with bolt-pull-out tests in Section 5. These tests also serve as a further means for validation of the proposed modeling technique.

## 2. Experimental material characterization of steel-wire-reinforced aluminum

In this section, material models including a description of material failure and fracture are deduced from experimental data. All specimens are taken from the extruded sections shown in Fig. 2. This section has two reinforced and two non-reinforced sides. Therefore, equal extrusion and cooling conditions for reinforced and non-reinforced aluminum are ensured.

**Table 1**
Chemical composition of the materials used – content in %.

| Elements | Si | Fe | Cu | Mn | Mg | Cr | Zn | Ti | Ni |
|---|---|---|---|---|---|---|---|---|---|
| EN AW-6060 | 0.455 | 0.219 | 0.027 | 0.059 | 0.404 | 0.001 | 0.005 | 0.015 | 0.003 |
| EN AW-6082 | 0.911 | 0.205 | 0.011 | 0.481 | 0.68 | 0.007 | 0.006 | 0.012 | 0.006 |
| Elements | C | Si | Mn | P | S | Cr | Ni | Mo | N |
| SS301 | 0.074 | 0.52 | 0.93 | 0.034 | 0.002 | 18.2 | 8.3 | 0.43 | 0.043 |

A spectral analysis of matrix material and steel wire elements gives the chemical compositions in Table 1. After extrusion, the section was cooled down in still air and aged at room temperature for at least 8 days, which results in an aluminum matrix in heat treatment state after fabrication T4(F) (DIN 29 850) [13]. This material is further referred to as "SWRA" (**S**teel-**W**ire-**R**einforced **A**luminum).

Prior to discussing the material properties in detail, an overview on the tensile behavior of SWRA compared to the non-reinforced aluminum matrix is given in Fig. 3. Tensile tests in extrusion direction (0°) of the non-reinforced aluminum matrix and of SWRA in wire direction were done, as well as transverse to the extrusion direction (90°) of the non-reinforced matrix and perpendicular to the wire direction for SWRA. The geometry of the specimens is shown in Fig. 11. In extrusion direction, the geometry follows the recommendations given by norm DIN EN ISO 6892-1 [14]. Due to the limited width of the extruded section, the geometry of the tensile specimens perpendicular to extrusion direction cannot follow the recommendations of the norm. The reference lengths for the specimens in extrusion direction is 15 mm and perpendicular to extrusion direction is 6 mm. The comparability between all specimens, thus, is given until uniform elongation and after that only persists for the specimens of each direction. It has to be noted, that for SWRA, the ordinate value "stress" is to be taken as force divided by the specimen's initial cross section.

Determining the reinforcement content of the specimens was done based on the ratio of steel-wire area related to the total cross-section area in the measuring zone. Since the aluminum is continuously reinforced, this can be taken as wire volume content. The calculated wire volume content of 3.1% leads to increased ultimate tensile strength in wire direction of 35% and a decrease in load carrying capacity perpendicular to wire direction. The higher tensile strength of the non-reinforced 90°-specimen compared to the 0°-specimen indicates an orthotropic plastic behavior of the aluminum matrix, introduced by the extrusion process.

The elastic properties are determined from the tensile tests of the aluminum matrix and are summarized in Table 2. Test data for the steel wires were provided by Merzkirch and further details on the test setup for tensile tests of steel wires is given at [9].

As all tests are performed under quasi-static conditions, and only a single strain rate is considered. Strain rate hardening therefore has been neglected. Experiments indicate plastic orthotropy of the aluminum matrix, which originates mainly from higher deformation degrees around the wires during the extrusion process. Different cooling and nucleation rates in the vicinity of the steel wire may also contribute to the plastic orthotropy. However, due to the experimental difficulties of testing plastic orthotropy in wires or of the aluminum matrix in the reinforced regions, plastic isotropy of wire and matrix had to be assumed.

With respect to these assumptions, the strain hardening properties and material failure and fracture are characterized in the following.

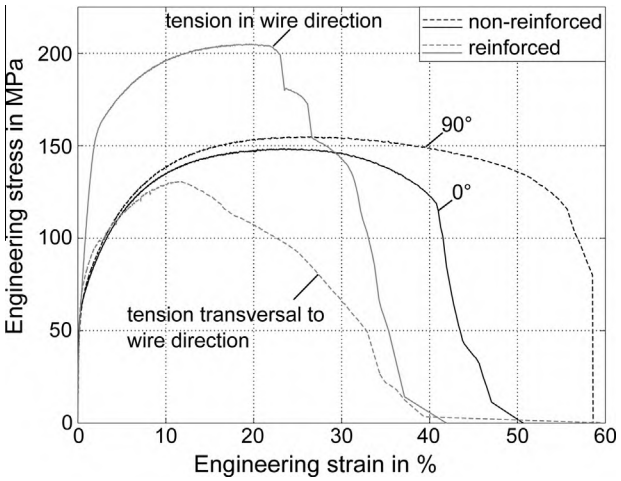


**Fig. 3.** Stress–strain curves of SWRA with a wire volume content of 3.1% and of non-reinforced aluminum EN AW-6060 (T4(F)).

**Table 2**
Elastic material properties.

| Property | Notation | Steel wire | Aluminum |
|---|---|---|---|
| Young's modulus $E$ in MPa | $E$ | 214,000 | 69,000 |
| Poisson's ratio | $\nu$ | 0.3 (estimated) | 0.33 |
| Yield strength in MPa | $R_{p0.2}$ | 1900 | 84 |
| Tensile strength in MPa | $R_m$ | 2050 | 148 |

### *2.1. Strain hardening properties of the aluminum matrix*

The strain hardening properties of the aluminum matrix are determined from tensile test data of non-reinforced aluminum. The tests are done in accordance with DIN EN ISO 6892-1 [14] and the derived strain hardening data is shown in Fig. 4.

As the tensile test data only gives valid information during uniform elongation up to a relatively low ultimate strain, an extrapolation of the strain hardening curve is necessary. For the aluminum alloy EN AW-6060, the Hockett–Sherby function [15] was chosen, as it gave reasonable predictions of the strain hardening behavior of the considered aluminum in other analyses [17,18].

The Hockett–Sherby function is

$$\sigma = \sigma_s - (\sigma_s - \sigma_y) \cdot \exp\left(-(N \cdot \varepsilon)^p\right) \tag{1}$$

where $\sigma_s$ is the saturation stress, $\sigma_y$ the yield stress, as well as $N$ and $p$ the fitting parameters.

These strain hardening parameters are often determined in an unconstrained least-squares fitting of the strain hardening function. However, with the experimental data losing its validity with the onset of necking at ultimate strain $\varepsilon_u$, the extrapolated data is uncertain. Constraining the fitting by adding Considèrés criterion improves the extrapolation by adding additional information to the fitting procedure [16,17]. The criterion is introduced to the fitting with two constraints

$$\left|\frac{d\sigma^{fit}}{d\varepsilon}\Big|_{\varepsilon=\varepsilon_u} - \sigma^{fit}(\varepsilon_u)\right| - \delta_1 \leqslant 0 \tag{2a}$$

$$\left|\sigma^{\exp}(\varepsilon_u) - \sigma^{fit}(\varepsilon_u)\right| - \delta_2 \leqslant 0. \tag{2b}$$

Constraint (2a) ensures that at the point of ultimate strain, Considèrés criterion is fulfilled within a certain limit $\delta_1$. Constraint (2b) ensures that the ultimate stress of the fitted function meets the experimental ultimate stress within the limit $\delta_2$. The identified parameters from the constrained fitting are summarized in Table 3.

Fig. 4 compares an unconstrained least-squares fit of the Voce function [19] (cf. Eq. (8)) to a constrained least-squares fit of the Hockett–Sherby function to experimental data of the considered aluminum alloy. Even though the fitted curves closely follow the experimental data, the extrapolated strain hardening data differs significantly. It can also be seen, that a least-squares fit without constraints does not assure fulfilling Considèrés criterion.

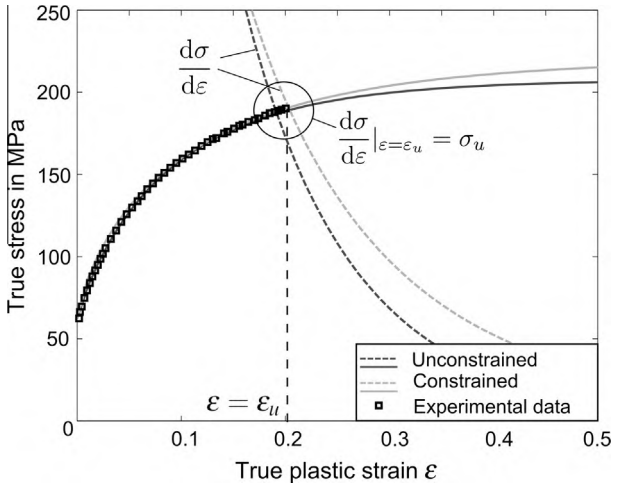


**Fig. 4.** Comparison between unconstrained fit of the Voce function and constrained fit of the Hockett–Sherby function.

**Table 3**
Strain hardening parameters for EN AW-6060 for the Hockett–Sherby function.

| Saturation stress $\sigma_s$ | Yield strength ($R_{p0.2}$) $\sigma_y$ | Hardening coefficient $N$ | Hardening exponent $p$ |
|---|---|---|---|
| 206.87 MPa | 54.36 MPa | 10.24 | 0.819 |

### *2.2. Description of material failure and fracture for the aluminum matrix*

The onset of wire debonding is linked to a change of the stress state in the aluminum matrix as a free surface is created at the interface. For the simulation of material failure and fracture at three-dimensional and varying stress states, the physically motivated Gurson model in its modification according to Tvergaard–Needleman [20,21] is used. This model considers fracture as a result of nucleation, growth and coalescence of inner voids, with the void growth depending on the stress state and material specific parameters. All simulations are done in LS-DYNA, (Livermore Software Technology Corporation LSTC, LS-DYNA Version 971, Revision 6.0.0) and the in LS-DYNA implemented Gurson model is described briefly. Eqs. (3)–(7) are taken directly from the LS-DYNA manual [32].

Failure is represented as a change in the Gurson flow function:

$$\Phi = \frac{\sigma_{eq}^2}{\sigma_Y^2} + 2q_1 f^* \cosh\left(\frac{3q_2\sigma_{Hyd}}{2\sigma_Y}\right) - 1 - (q_1 f^*)^2 = 0 \tag{3}$$

With $\sigma_{eq}$ being the von Mises equivalent stress, $\sigma_y$ is the yield stress and $\sigma_{Hyd}$ is the hydrostatic stress. $q_1$ and $q_2$ are fitting parameters. $f^*$ is the effective void volume fraction, which is [21]

$$f^*(f) = \begin{cases} f & f \leqslant f_C \\ f_C + \frac{1/q_1 - f_C}{f_F - f_C}(f - f_C) & f > f_C \end{cases} \tag{4}$$

where $f_F$ and $f_C$ are material parameters with $f_F$ the fracture void volume fraction. $f_C$ is the critical void volume fraction, which defines the onset of void aggregation. $f$ is the present void volume fraction which develops according to

$$\dot{f} = \dot{f}_G + \dot{f}_N. \tag{5}$$

The rate of the void volume fraction $\dot{f}$ consists of growth of existing voids $\dot{f}_G$ and nucleation of new voids $\dot{f}_N$. Void growth is described in the modification by [12], so that voids are allowed to grow also under zero mean stress conditions (i.e. shear dominated load cases).

$$\dot{f}_G = (1-f)\dot{\varepsilon}_{kk}^p + k_\omega \omega(\underline{\sigma}) f(1-f)\dot{\varepsilon}_{eq}^p \frac{\sigma_Y}{\sigma_{eq}}. \tag{6}$$

$\omega(\sigma)$ distinguishes shear stress states from axisymmetric stress states, ensuring that void growth is only modified for shear stress states. $k_\omega$ is a fitting parameter determined from experiments under pure or simple shear stress states [12].

The nucleation of new voids is linked to the equivalent plastic strain by a normal distribution of $f_N$ where $f_N$ is the volume fraction of nucleating particles, $\varepsilon_N$ a mean strain for nucleation and $S_N$ is the standard deviation of $\varepsilon_N$.

$$\dot{f}_N = \frac{f_N}{s_N\sqrt{2\pi}} \exp\left(-\frac{1}{2}\left(\frac{\varepsilon_{eq}^p - \varepsilon_N}{s_N}\right)^2\right) \cdot \dot{\varepsilon}_{eq}^p. \tag{7}$$

The Gurson model with shear modifications by Nahshon and Hutchinson in total has nine parameters $q_1$, $q_2$, $f_0$, $\varepsilon_N$, $S_N$, $f_N$, $f_C$, $f_F$ and $k_\omega$, which must be determined. This is done with tensile test data for the identification of the first eight parameters and shear test data for $k_\omega$, leading to high effort for the identification process. In addition, the material parameters are non-unique [23], and only one set of parameters allows for a physical-microstructural interpretation. Therefore, narrow boundaries for the parameters are chosen.

For the constitutive parameters, $q_1 = 1.5$ and $q_2 = 1$ often give good results [24–26]. The initial void volume fraction $f_0$ can be assessed by evaluation of micrographs and commonly ranges from $0.001 < f_0 < 0.08$ [25].

The critical void volume $f_C$ is discussed controversially in the literature. According to [21], $f_C$ is between $0.15 < f_C < 0.2$. [25], in contrast, gives $0.03 < f_C < 0.15$ as bounds for the critical void volume. [26] reports $f_C$ as low as $f_C \approx 0.03$. [27] found that for small values of $f_0$, $f_0$ and $f_C$ are dependent on each other and that for any initially assumed $f_0$, a corresponding $f_C$ can be found, leading to equal material behavior.

$f_F = 0.25$ is often chosen, as final fracture shows only little sensitivity toward $f_F$ [25–27]. This is due to a quickly rising void volume fraction when $f$ reaches $f_C$. Here, $f_F = 0.25$ is used as an upper bound value.

The parameters for void nucleation $\varepsilon_N$, $S_N$ and $f_N$ can be linked to the onset and evolution of necking in the uniaxial tensile test [21]. However, the nucleation parameters $f_N$, $\varepsilon_N$ and $S_N$ are strongly dependent on the material so that an estimation is difficult. Particles causing void nucleation in the aluminum matrix can be inclusions or precipitates and their micrographical

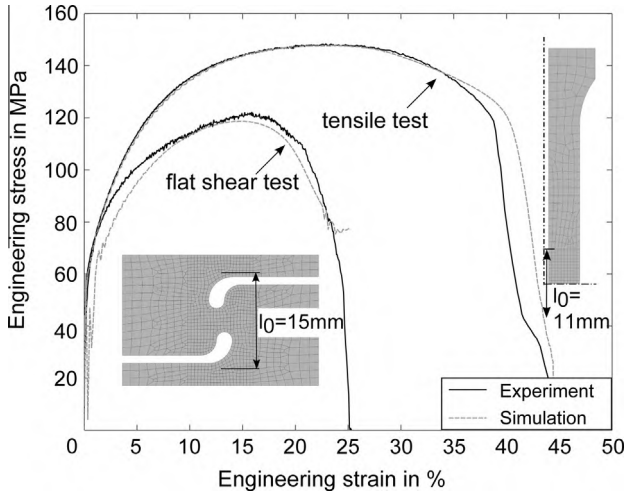


**Fig. 5.** Experimental and simulated stress–strain curves with optimized Gurson material parameters.

**Table 4**
Gurson material fracture parameters for EN AW-6060 for a characteristic element length of $l_c$ = 0.5 mm.

| Parameter | $q_1$ | $q_2$ | $f_0$ | $\varepsilon_N$ | $S_N$ | $f_N$ | $f_C$ | $f_F$ | $k_\omega$ |
|---|---|---|---|---|---|---|---|---|---|
| Lower bound | 1.0 | 0.9 | 0.001 | 0 | 0 | 0 | $>f_0+f_N$ | $>f_C$ | 0 |
| Upper bound | 1.5 | 1.0 | 0.08 | – | – | 0.1 | 0.2 | 0.25 | 3.0 |
| Model value - chosen (c) or identified (i) | 1.5 (c) | 1.0 (c) | 0.0033 (i) | 0.28 (i) | 0.0311 (i) | 0.024 (i) | 0.032 (i) | 0.21 (i) | 0.6 (i) |

analysis gives guiding values for $S_N$ and $f_N$. Micrographs of the aluminum matrix show a content of precipitates of about 2.5%, which is in accordance with the identified content of void nucleating particles.

The parameter $k_\omega$ governing shear fracture is determined with the help of flat shear specimens [28] (see Fig. 5) using the by Nahshon given upper limit of $k_\omega < 3$ [12]. These limits for the Gurson parameters, and the identified parameters for the aluminum matrix are summarized in Table 4. The void nucleation and growth parameters are taken as being dependent on the characteristic element length which is here $l_c$ = 0.5 mm.

Fig. 5 depicts experimental stress–strain curves for tensile and shear test of the non-reinforced aluminum matrix together with stress–strain curves from the numerical fitting procedure. Further, the geometry of the testing specimens with reference lengths for the determination of the strain value is shown. In the fracturing region, the specimens are meshed such that the characteristic element length is kept close to $l_c$ = 0.5 mm. As the Gurson model is only implemented for the explicit LS-DYNA solver, the quasistatic conditions of the experiment could not be met. The tensile test was simulated at a velocity of $v$ = 1 m/s, the shear test was simulated at $v$ = 1.33 m/s. Due to this, some dynamic jitter can be seen in the simulation data. However, the kinetic energy in the simulations was always below two percent of the total energy, so that no major inertia effects influence the material's response.

The identified Gurson parameters lead to a good agreement in the tensile test data (cf. Fig. 5), considering stress-level, onset of failure and evolution of fracture. The differences in the fracture evolution is less than the observed experimental scatter within five tested tensile specimens. Using the Nahshon–Hutchinson modification for shear fracture, the shear test data is also captured quite well. The divergence in the hardening behavior is attributed to the fact, that the Gurson model does not take orthotropic plastic behavior into account. Therefore, the hardening behavior with an uniaxial stress-state matches well, whereas the simulated hardening in the shear test differs. Maximum strength, failure onset and fracture evolution, though, are also captured well for the shear specimen. A complete rupture as in the experiment does not occur in the simulation. After the deletion of the first fracturing elements, some elements in the shearing region become highly distorted and are no longer deleted. A smaller element size with a characteristic length of $l_c$ = 0.25 mm was tested and improved this shortcoming, however, the element length of $l_c$ = 0.5 mm was kept in order to maintain shorter calculation times.

### *2.3. Strain hardening properties of the steel wire*

The steel wires are mainly stressed axially with the loads being transferred as interface shear loads. For tension perpendicular to the wires, early debonding is visible so that the magnitude of different stress states is limited. The assumption of a

maximum strain criterion is justifiable, since the fracture criterion is calibrated on the prevailing fracture mechanism of the wires.

As the material data for the steel wires has to be assessed in a non-embedded state, the steel wires fail due to necking at comparably low strains of about 2%. Therefore, the experimental data for the determination of the strain hardening curve is very limited. As the experimental data indicates a saturation of the strain hardening curve at ultimate stress (cf. Fig. 6), a nearly perfectly plastic extension after ultimate stress is reasonable. The extension is done with the Voce function, which is [19].

$$\sigma = \sigma_S - (\sigma_S - \sigma_y)\exp\left(-\frac{\varepsilon}{\varepsilon_0}\right). \tag{8}$$

The determined strain hardening parameters of the Voce function are given in Table 5.

### 2.4. Description of material fracture for the steel wire

Tensile test results for SWRA in wire direction shown in Fig. 3 reveal that necking and fracture of the wire starts at much higher strains than in a non-embedded wire. This is due to a supporting effect of the interface on the wire's surface, which does not allow for necking. The margin of stress states acting on the steel wires is narrow and mainly axial load prevails. Hence, the phenomenological maximum strain criterion is used which is calibrated based on the area of reduction of the cross-section of embedded wires. The area of reduction is measured at the fractured wires from reinforced tensile specimens shown in Fig. 11a. The fracture strain is defined as

$$\varepsilon_f = \ln\left(\frac{A_0}{Af}\right) \tag{9}$$

where $A_0$ is the initial cross-section area of the steel wire and $A_f$ is its minimal cross-section area after fracture. For SWRA, the fracture strain of the steel wires was assessed by the evaluation of the fractured surface to $\varepsilon_f \approx 0.7$.

### 2.5. Experimental characterization of wire-matrix interface

Fig. 7 depicts an exemplary microstructure of a steel wire composite (EN AW-6082 reinforced with SS301) showing the vicinity of the steel wire. The specimen shows a fine grain formation with an even finer microstructure around the steel wire and along the longitudinal weld seam due to the higher local degree of deformation during the composite extrusion process. As a result of the Barker-Etching method the steel wire shows some discoloration. It is also visible that the interface provides

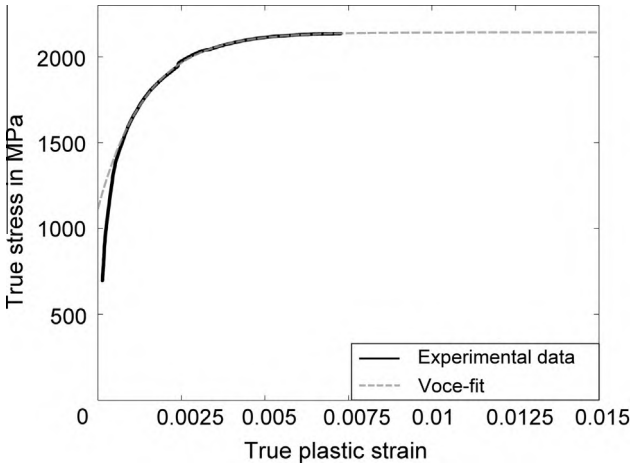


**Fig. 6.** Experimental strain hardening function of the steel wire and approximation with the Voce function.

**Table 5**
Voce strain hardening parameters for the high-strength steel wires.

| Saturation stress $\sigma_s$ | Yield strength $\sigma_y$ | Prestrain $\varepsilon_0$ |
|---|---|---|
| 2143 MPa | 1115 MPa | 0.00143 |

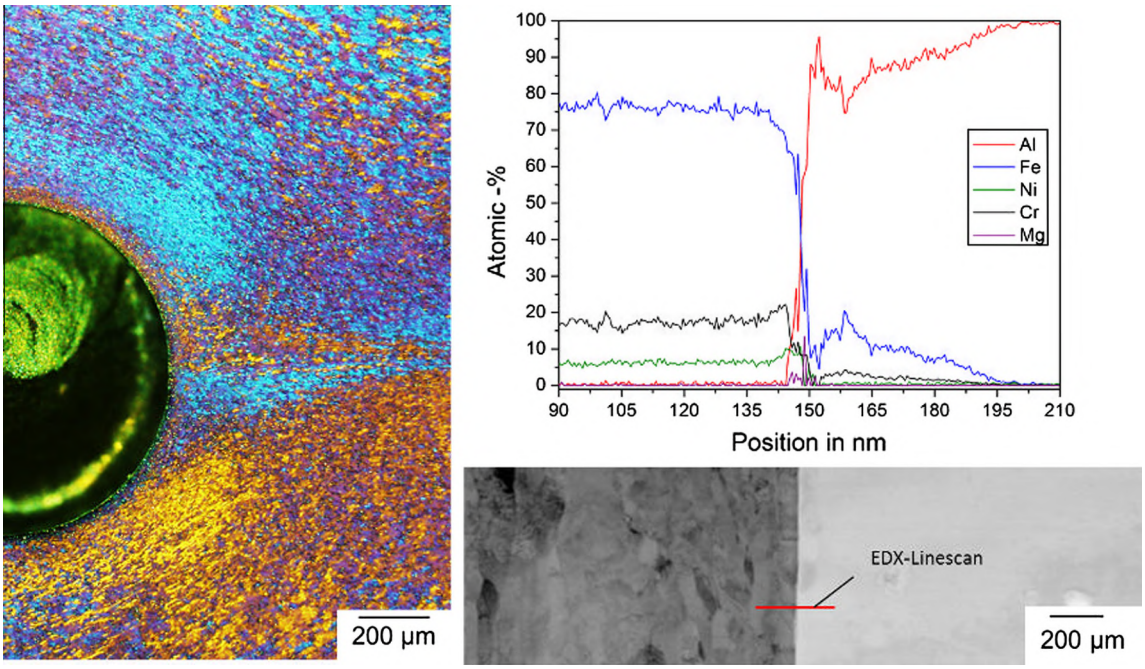


**Fig. 7.** Left: Microstructure around the steel wire (Barker-Etching, magnification 100:1) right: TEM image with EDX linescan across the interface.

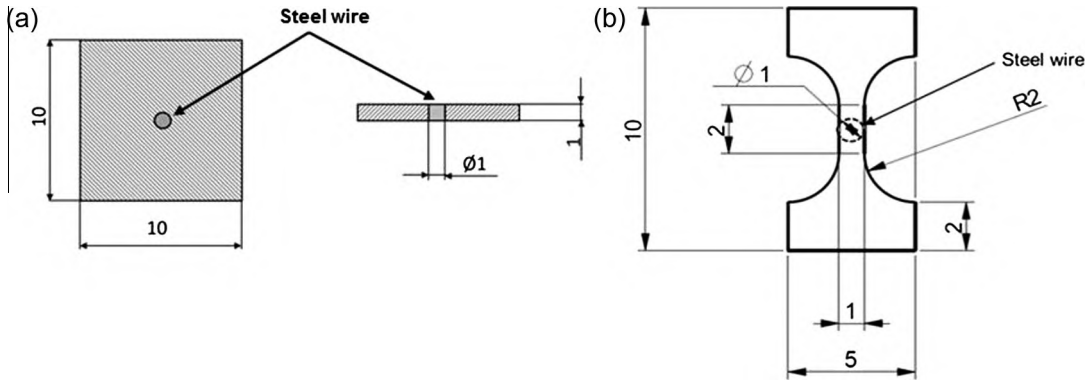


**Fig. 8.** Specimen geometries: (a) Push-out test (b) Interface-tensile test.

a good bonding, free of mesoscopic defects. The right part of Fig. 7 shows a TEM-Image of the interface with a seamless bonding. Additional EDX analysis reveals a chemical bonding with diffusion of Fe, Cr and Ni in a zone of 5–100 nm. Previous investigations showed the same interface condition with diffusion zones up to 250 nm for an EN AW-6060 alloy [10].

The mechanical interface properties were analyzed by push-out-tests [29,30] in order to determine the debonding shear strength and by tensile tests, determining the debonding normal strength. The geometries of the specimens are shown in Fig. 8. During the push-out-test, an indenter pushes directly onto the steel wire, while the surrounding matrix is supported, in order to minimize bending loads. The debonding shear strength is calculated as maximum force divided by interface area.

For the cutting of the specimens for the interface-tensile tests, wire eroding was used. This allows for an accurate preparation of the specimen with exact alignment of the wire, lying in the gauge length of the specimen. The debonding normal strength is calculated as maximum force divided by fractured surface, which equals to the wire surface as the failure of the specimen is located directly in the zone of the interface.

The measured debonding shear strength is 96.1 MPa and the measured debonding normal strength is 10.9 ± 1.25 MPa. Both determined values are lower than the maximum strengths as they are average values over the fracturing region [31].

## 3. Modeling of steel-wire-reinforced aluminum for numerical analysis

Focusing on the analysis of the interface between aluminum matrix and steel wire, a detailed volume model as shown schematically in Fig. 9 is essential. Steel wire and aluminum matrix are modeled in a three dimensional volume representation and connected with cohesive elements along the surface of the wire. All experimented specimens show a misalignment of the wires. This misalignment is caused by the extrusion process and is represented in the simulation models. The element size with a small characteristic element length of $l_c = 0.5$ mm is necessary in order to have a reasonable well representation of the geometry of the wires.

It is evident that this detailed modeling can only be done on the scale of small specimens and a discretization of larger structures with this element size quickly leads to large calculation times. Therefore, [2] introduced a homogenized shell model for SWRA which yields accurate results for structural strength analysis. For the simulation of material fracture in SWRA, a simplified shell-beam model of SWRA gives good results in load cases with dominating tension in wire direction [6], where interface failure has only minor influence.

The experimentally determined debonding strengths are used in an interface model, which takes pre- and post-debonding interface properties into account and is described in the following.

### 3.1. Cohesive interface model

A model of the interface of SWRA has to tightly bond the steel wire to the aluminum matrix as experimentally no sliding between wire and matrix can be seen up to the point of wire debonding. After debonding, there still remains friction between wires and matrix and depending on the straining of the matrix, a pinching of the wires occurs. Thus, the interface model is two-staged.

In the first stage up to debonding, the interface is modeled using cohesive elements (LS-DYNA ELFORM19 four point, eight node cohesive element). After debonding, a frictional contact is established, which accounts for friction forces and pinching. The stage of cohesion is modeled with an elastic cohesive material model (MAT_COHESIVE_ELASTIC). It distinguishes an in-plane (tangential) stiffness and an out-of-plane (normal) stiffness. For reasonably thick cohesive layers, these stiffnesses can be determined experimentally. For SWRA, the interface between aluminum matrix and steel wire is almost of zero thickness and the stiffnesses have to be estimated. Not allowing for a sliding motion at the interface, normal stiffness $E_N$ and tangential stiffness $E_T$ are set to 10 times of the wire's elastic stiffness to $E_T = E_N = 2 \cdot 10^6$ MPa. The interface is assumed to fail, once a limit of normal interface stress is reached. Thus, the failure condition is

$$\sigma_n \leqslant \sigma_{n,\max}. \tag{10}$$

Decohesion due to in-plane shear stresses is excluded for several reasons. As the experiments show, the interface's shear strength is with $\tau_{\max} = 96$ MPa significantly higher than its normal strength with $\sigma_{n,\max} \approx 11$ MPa. Decohesion due to shear loads is thus less critical than due to normal stresses. For the circular wire interface, the chosen discretization influences the interface's stress state which does not allow for an iso lated view on either normal interface stresses or hoop shear stresses. Eq. (10) should thus be interpreted as a phenomenological numerical failure criterion rather than a physically accurate description of failure.

### 3.2. Influence of discretization on the interface stresses

Due to a limited fineness of the numerical representation of the interface between wire and matrix, pure hoop shear stresses also result in an artificial normal stress component and vice versa.

Consider the discretization of steel wire and matrix (Fig. 10a) as well as a stress state of exclusive hoop stress at the interface. This may occur if the wire is twisted inside the matrix. As this is a state of pure in-plane shear stress, no normal stresses occur. The shear forces acting on the interface $F_T$ are shown in Fig. 10b. However, due to discretization effects, the shear

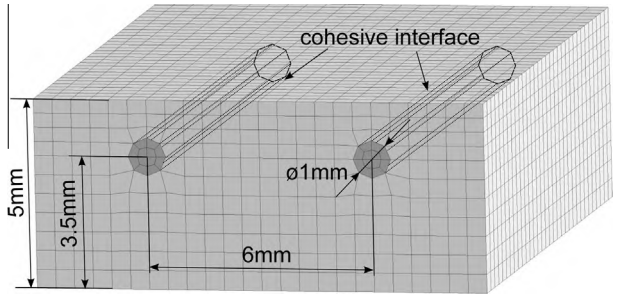


**Fig. 9.** Detail of a three dimensional finite element model of SWRA.

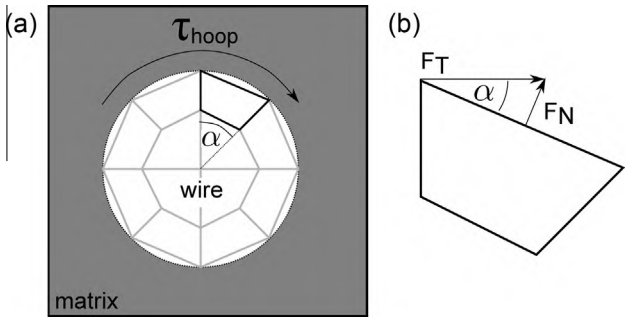


**Fig. 10.** (a) Discretization of the circular interface with a discretization angle $\alpha = 45°$ (b) Resulting forces from pure hoop stress for the given discretization.

forces lead to artificial normal forces $F_N$. The general relation between shear forces and resulting normal forces depending on the discretization angle $\alpha$ is

$$F_N = F^T \cdot \sin(\alpha) \quad \text{or} \quad \sigma_n = \tau_{hoop} \cdot \sin(\alpha) \overset{\alpha=45^\circ}{\approx} 0.71 \cdot \tau_{hoop} \tag{11}$$

With a smaller discretization angle, a better separation of normal and shear forces can be reached, but for reasons of computational efficiency, $\alpha$ is kept at 45°. However, for the analysis of interface failure in SWRA in Section 4, the discretization angle is reduced to $\alpha = 22.5°$ in order to have a better separation of normal forces and shear forces.

### *3.3. Contact model for post-debonding interface*

Once the steel wire has debonded, a frictional contact between wires and matrix is established. This contact is essential as the wires do not allow for a free deformation of the matrix. Hence, the contact changes the stress state in the matrix by transferring compressive loads.

For numerical simulation, the post-debonding contact is considered by using a segment based erosive contact in LS-DYNA (∗CONTACT_ERODING_SINGLE_SURFACE). Especially for edge-to-edge contact, the segment based contact is advantageous over a standard node penalty based contact at detecting penetrations [22]. Sticking friction coefficient $\mu_S$ and slipping friction coefficient $\mu_G$ are chosen as 0.61 and 0.47, respectively [33].

## 4. Analysis of debonding in steel-wire-reinforced aluminum

For the study of interface stresses and onset of debonding, two scenarios are considered. In the first scenario, a tensile test of SWRA with elongation in wire direction is analyzed. In the second scenario, a tensile test with elongation perpendicular to wire direction is examined. All specimens are waterjet-cut from the reinforced part of the extruded sections shown in Fig. 3. The size of the wrought material limits the specimen's geometry, so that for the tensile specimens perpendicular to wire direction, a standard geometry is not fabricable. The geometry of the specimens is shown in Fig. 11. Each test is repeated with at least four specimens.

### *4.1. Interface stresses at tension in wire direction*

The tensile specimens of SWRA are tested and the displacement field is recorded with an optical measurement system (GOM Aramis). This allows for the determination of the deformation field on the surface of the specimens. The reference length for strain measurement was chosen as $l_0 = 15$ mm and all specimens necked and failed within the gauge length.

The simulations were done with a symmetrical model of the experimental specimen and the development of interface normal stresses is shown for an elongation in wire direction in Fig. 12. The process can be divided into four phases:

(i) Elastic compression due to differing Poisson's ratios of steel wire and aluminum matrix
(ii) Nearly stress-free state when steel wire and matrix both deform plastically with strain ratios of 0.5 (plastic volume conservation)
(iii) Increasing normal tensile stress after onset of necking of the matrix
(iv) Interface failure.

Until necking of the matrix, corresponding necking and fracture of the wire are avoided, as a local reduction of the wire's cross-section is blocked by the tight bond of the interface. Thus, the high strength of the wires can be used for reinforcement of the aluminum matrix over a wide strain range.

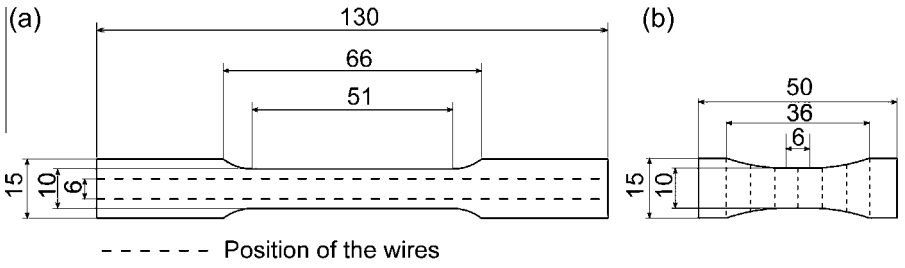


**Fig. 11.** Specimen geometry of SWRA for tensile tests (a) in wire direction (b) perpendicular to wire direction.

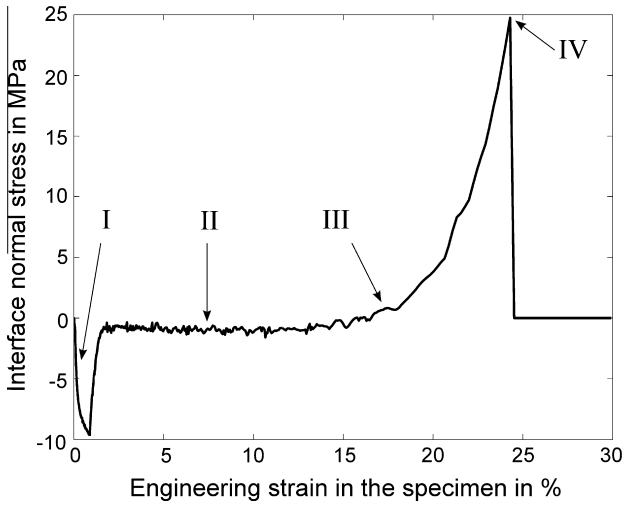


**Fig. 12.** Development of interface normal stress in SWRA for elongation in wire direction.

After onset of necking in the matrix, the normal stress in the interface rapidly rises. Thus, higher interface normal strengths have a limited effect on the onset of wire debonding. A numerical assessment of the failure behavior of SWRA at varying interface strengths was completed, confirming a low sensitivity of the material toward interface normal strength at pure axial tension. Three normal strengths, 25 MPa, 50 MPa and 75 MPa were simulated and the stress–strain curves are compared with experimental data in Fig. 13. As the material is inhomogeneous, the shown stress level should be taken as

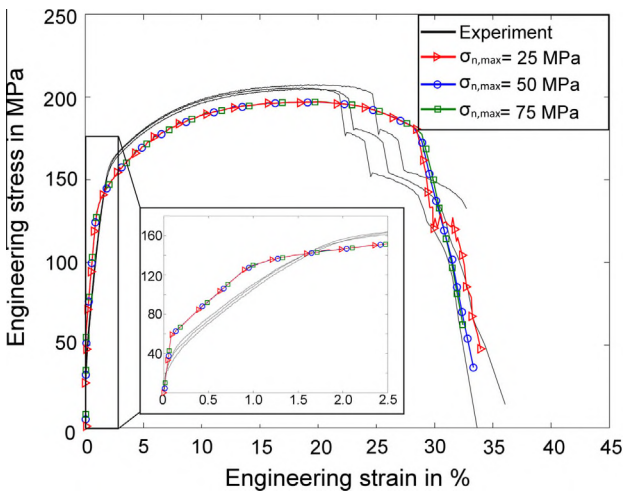


**Fig. 13.** Sensitivity of SWRA toward interface normal strength at tension in wire direction.

tensile force divided by initial cross-section of the specimens. The simulations confirm the small sensitivity of the fracture in pure tension in wire direction toward interface normal strengths.

### 4.2. Discussion of the tensile test results in wire direction

Comparing simulated stress–strain curves with the experimental data from three tensile tests Fig. 13, an overall good agreement can be stated. Particular differences are discussed in the following.

#### 4.2.1. Differences in elastic and elasto-plastic region ($\varepsilon < 2\%$)

In the first part of the tensile test, steel wire and aluminum matrix start to deform elastically. This is followed by the aluminum matrix deforming plastically while the steel wire still deforms elastically. This is visible as the first bend in the stress–strain curve (at about $\sigma = 40$ MPa). The second bend marks the onset of plastic deformation of the steel wire (at about $\sigma = 160$ MPa). In both parts, the slope of the simulated curve does not agree, as the simulation does not take thermal residual stresses into account. These thermal residual stresses arise in the extrusion process during cooling from extrusion temperatures of $T = 450$–$550$ °C and lead to high axial stresses due to differing coefficients of thermal expansion of matrix and wire. The tensile stresses in the aluminum matrix range from 15 MPa to 90 MPa in the vicinity of the wire, the compressive stresses in the wire are at about 1000 MPa. Consequently, a partial plastification of the aluminum matrix around the steel wire occurs [6]. The pre-stressed material shows a lower stiffness and a lower elastic limit for a further tensile load in wire direction.

#### 4.2.2. Differences in the plastic part ($2\% < \varepsilon < 20\%$)

With both wire and matrix undergoing plastic deformation, the elastic residual stresses are released. However, a difference in simulated and experimental stress level of maximally 5% remains. A higher yield stress and plastic hardening in the experimental data could be attributed to the grain refinement of the aluminum matrix around the steel wires, during the extrusion process. The micrograph in Fig. 7 confirms a finer grain size around the steel wires which act as condensation nuclei for a heterogeneous grain formation. The simulation does not account for the changed plastic strain hardening properties of the aluminum matrix in this region.

#### 4.2.3. Differences in failure and fracture ($20\% < \varepsilon$)

The simulated data predicts necking at the same necking strain as the experimental data. Necking starts in the aluminum matrix and the interface fails due to quickly rising normal interface stresses. The released wire starts to neck and fractures. The moment of wire fracture can be seen as a distinct drop in the force, which is predicted at higher strains than in the experiment. The shown simulated data is obtained with a wire fracture strain of $\varepsilon_f \approx 0.4$ which is lower than the experimental wire fracture strain of $\varepsilon_f \approx 0.7$. Using $\varepsilon_f \approx 0.7$ led to an overestimation of overall fracture strain, so that a lower value was chosen. Here, one has to bear in mind, that the wire can only reach a high fracture strain due to the supporting effect of the interface. It is likely to have a high void content already before onset of wire necking, which might justify taking a lower fracture strain for the phenomenological fracture criterion.

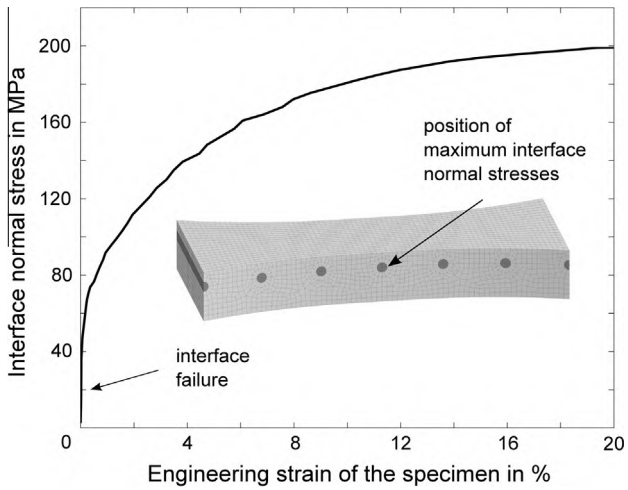


**Fig. 14.** Development of interface normal stresses in SWRA for tension perpendicular to wire direction.

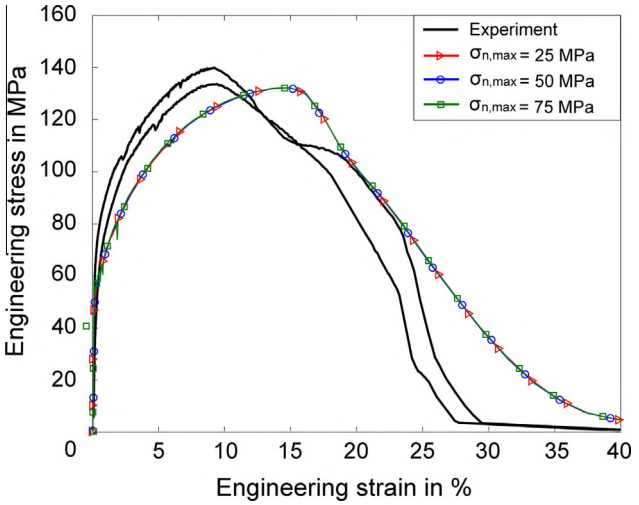


**Fig. 15.** Sensitivity of SWRA toward interface normal strength at tension perpendicular to wire direction.

### *4.3. Interface stresses at tension perpendicular to wire direction*

For tension perpendicular to wire direction, the wire acts similar to a non-deformable rigid body, due to its comparably high Young's modulus and yield strength. Hence, the maximal interface normal stresses increases related to the strain hardening of the aluminum matrix as depicted in Fig. 14. This leads to an almost immediate debonding of the wires, which was detected with an optical measurement directly looking at the wire-matrix interface of the specimen shown in Fig. 11b.

At tension perpendicular to wire direction, the interface normal stresses rapidly rise and the interface fails early. Therefore, the simulated stress–strain curve of SWRA shows almost no sensitivity toward interface normal strength (cf. Fig. 15). The differences between simulated and experimental data indicates plastic orthotropy of the reinforced aluminum matrix, which was not considered for simulation. Further, the grain refinement of the matrix due to the introduction of the wires may add to the differences between test and simulation.

## 5. Fracture behavior of steel-wire-reinforced aluminum

After verifying the material modeling and simulation technique in Section 4, good agreement between simulation and experiment motivates further analysis of SWRA on a component level. In order to determine the influence of wires and wire debonding on the fracture behavior of SWRA, a bolt-connection is tested and simulated. A comparison is drawn to the fracture behavior of the non-reinforced aluminum matrix. A scheme of the experimental test setup and the corresponding simulation model is shown in Fig. 16.

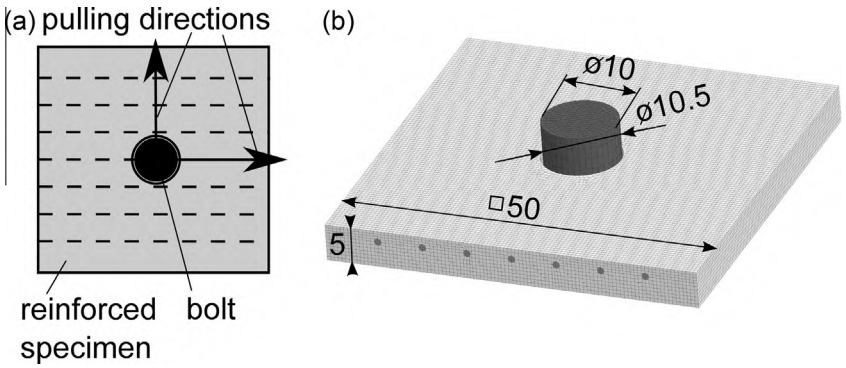


**Fig. 16.** (a) Scheme of the bolt-pull-out test (b) corresponding simulation model.

### 5.1. Experimental setup of the bolt-pull-out test

The suggested bolt-pull-out test is similar to a pin-bearing strength test. However, the test is not stopped once a certain hole-extension is reached, instead the bolt is pulled out until final rupture of the specimen. This way, this test can give information on the performance and fracture behavior of bolt-connections. Additionally, it provides a complex load scenario for further validation of the proposed modeling technique.

For experimental testing, the specimens are cut from the section shown in Fig. 3. A hardened high-strength steel bolt of 10 mm diameter is then inserted into a hole of diameter 10.5 mm and pulled through the material. The specimens are held using wedge grip jaws and the bolt displacement is recorded with the optical measurement system. Further, the displacement of the wedge grip is recorded, in order to consider the deformation of the testing machine and a slipping of the wedge grips. Especially for the bolt-pull-out test perpendicular to wire direction, the clamping length of the specimen is limited and a sliding of the gripping wedges was observed. However, the grips held the specimens until final rupture.

For all tests, at least four specimens were tested. It should be noted, that the bolt-pull-out tests were carried out five months later than the tensile tests for parameter identification of the material model. However, a natural ageing of the aluminum alloy, which leads to higher strengths of the aluminum matrix in the bolt-pull-out tests, can be anticipated.

### 5.2. Comparison of fracture behavior of steel-wire-reinforced aluminum and non-reinforced aluminum

Testing non-reinforced aluminum allows for a comparison to the fracture behavior of SWRA. Assuming isotropy of the aluminum, only one pull-out-direction is tested and simulated. As load and specimen are symmetrical, symmetrical simulation models are used. A minimum of four specimens was tested for each test.

#### 5.2.1. Bolt-pull-out in non-reinforced aluminum

At the bolt-pull-out test in non-reinforced aluminum, two fracture modes can be observed. First, a ductile fracture develops due to necking in tension state close to the middle of the hole. For one specimen, this ductile fracture developed into a long crack perpendicular to the loading axis until a sudden shear off in loading direction occurred. For two other specimens, the initial crack turned into the pull-out direction (direction of maximum shear), resulting in a shear off fracture. One specimen failed exclusively in a shear fracture mode.

The simulation model correctly predicts an initial ductile fracture shortly above the middle of the hole. The initiated crack turns into the direction of maximum shear stress until a sudden shear off sets in. It should be mentioned, that the evolution of the crack seems influenced by the regular meshing of the specimen which favors one crack direction. However, with an element size of $l_c = 0.5$ mm this can hardly be avoided. Fig. 17 shows a comparison between simulated and experimental fracture.

A comparison of simulated and experimental force–displacement curve for three experimental specimens is drawn in Fig. 18. The experimental data of the fourth specimen was lost due to a system error of the measurement system. The general trend of the force–displacement curve matches the experimental data, also the final rupture is predicted satisfactory. However, the force-level is underpredicted by more than 10%. Probable reason for this is an inherent plastic orthotropy in the extruded aluminum (cf. Fig. 3). For a better numerical prediction, a modification of the Gurson model for orthotropic yield for instance with a Barlat yield function [34] could lead to better results. An approach to coupling of an orthotropic yield function to the Gurson fracture description can be found at [35]. Another reason for this is a natural ageing of the aluminum alloy given the time between parameter identification of the material model and the bolt-pull-out tests.

#### 5.2.2. Bolt-pull-out in wire direction

Testing the reinforced aluminum in wire direction, an initial crack perpendicular to wire direction develops due to necking similar to the non-reinforced aluminum specimens. This crack is arrested for all tested specimens by the introduced

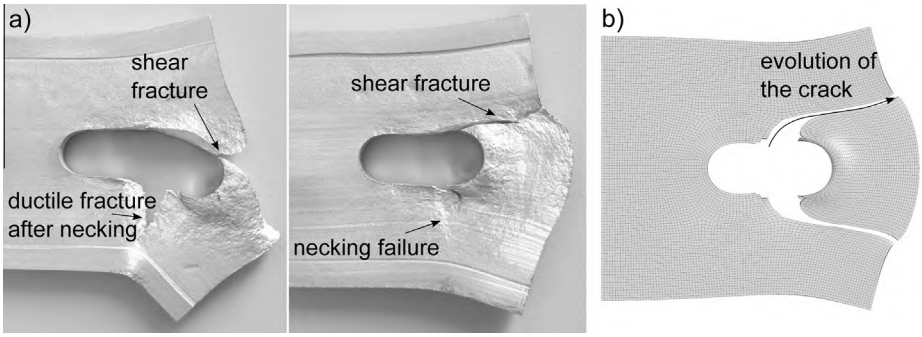


**Fig. 17.** (a) Experimental and (b) simulated fracture for a bolt-pull-out test of non-reinforced aluminum.

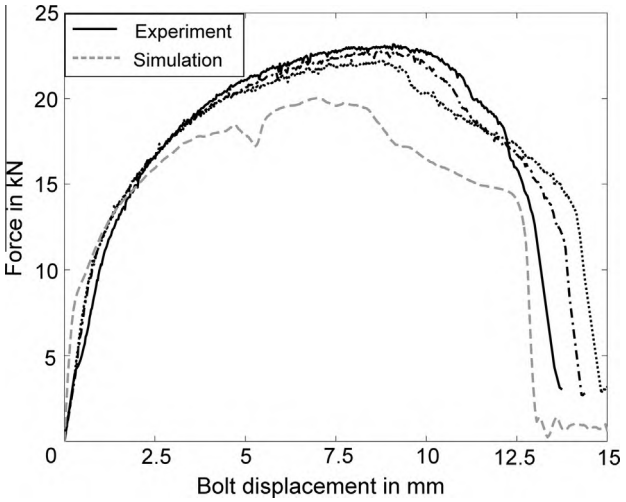


**Fig. 18.** Experimental and simulated force–displacement curve for a bolt-pull-out in non-reinforced aluminum.

wires. The subsequent shear fracture is similar to the fracture in non-reinforced aluminum. It runs along the steel wire, which supports the evolution of the shear crack. For several specimens, the crack arresting wire fractured during testing. The wire fracture is predicted by the simulation and it should be noted, that at this stage, the interface has already failed completely. The forces leading to the wire fracture have to be transferred via the frictional contact.

In two experimented specimens, fracture set in along the middle wire and the matrix fractures after a ductile necking process. The two observed fracture types are shown in Fig. 19 and are compared to the simulated fracture. These mechanisms explain an earlier drop in the force–displacement curve compared to non-reinforced aluminum, as can be seen in Fig. 20a. The simulated data is in good agreement with the experimental one, as it lies within the experimental scatter of the test data. Maximum force, onset of fracture and crack propagation is well predicted.

*5.2.3. Bolt-pull-out perpendicular to wire direction*

Reinforcing perpendicularly to the pull-out direction weakens the specimen significantly and changes the fracture mode compared to non-reinforced aluminum. An early debonding of the middle wire element creates a void in the aluminum matrix which leads to the formation of a neck. Subsequently, a crack propagates through the matrix along the middle wire element. As the matrix is predamaged by the created void, the ductile fracture mode of the aluminum matrix is supported and the crack propagation is faster. A comparison between simulated and experimental force–displacement curve is shown in Fig. 20b and fracture is compared in Fig. 21. A difference in experimental and simulated maximum force shows a maximum of 10%. Besides the already discussed matrix properties, this may also be attributed to a relatively coarse meshing of the wires and the surrounding matrix. With the wire debonding from the matrix, an edged void results, as a circular hole cannot be represented. Then, a smooth neck cannot develop and the fracture process is premature. The crack propagation with a sudden final rupture is predicted well.

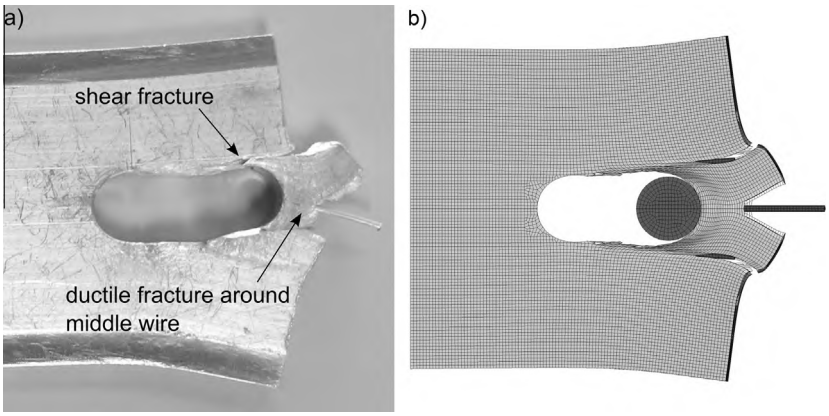


**Fig. 19.** (a) Experimental and (b) simulated fracture for a bolt-pull-out test in wire direction of SWRA.

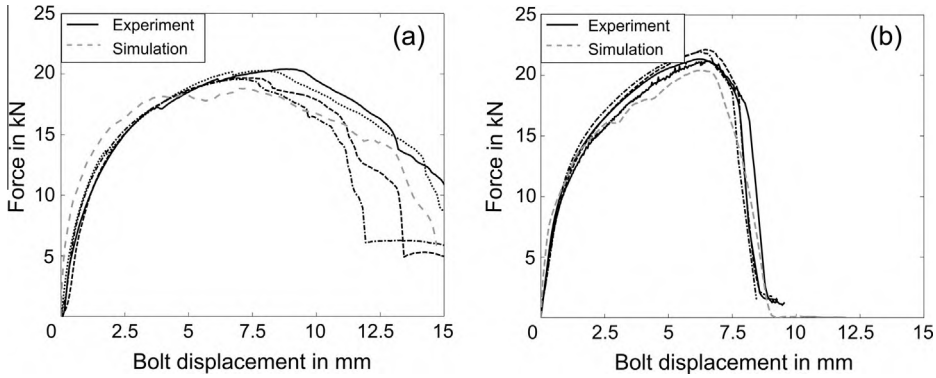


**Fig. 20.** (a) Experimental and simulated force–displacement curve of bolt-pull-out test in wire direction, (b) experimental and simulated force–displacement curve of bolt-pull-out test perpendicular to wire direction.

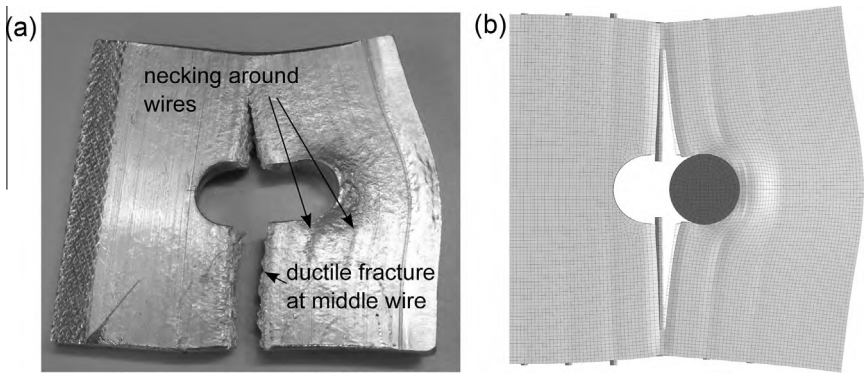


**Fig. 21.** (a) Experimental and (b) simulated fracture for a bolt-pull-out test perpendicular to wire direction of SWRA.

## 6. Summary and conclusion

Reinforcing an aluminum matrix with high-strength steel wires leads to a considerable increase in the composite's ultimate tensile strength. Adding a low wire content of 3.1% leads to an increase in ultimate tensile strength of about 35%. An inherently low fracture strain of the steel wires is increased due to a supporting effect of the interface between aluminum matrix and steel wire. Thus, the high strength of the wires can be used in pure tension up to high tensile strains of about 20%. For stress states differing from pure tension in wire direction, debonding of the wires is an important mechanism of material failure and was investigated in this research.

Debonding strengths were measured experimentally and serve for calibration of a suggested modeling technique for SWRA. It was shown, that wire debonding for pure tension in wire direction is caused by an onset of necking in the surrounding matrix, whereas wire debonding at tension perpendicularly to wire direction is caused by the difference in stiffness and yield strength of wire and matrix. The arising normal interface stresses are then related to the strain hardening of the matrix. For both discussed mechanisms, significantly postponing debonding by increasing the interface's normal strength is not possible. This was proven in sensitivity analyses of the tensile tests in and perpendicular to wire direction, varying the interface's normal strength. After debonding, however, loads are still transferred to the wire by frictional contact, with the contact also changing the stress state of the matrix by transferring compressive loads. It should be noted that in all simulations, the interface normal stresses reach the limit normal stress before the shear stresses reach the experimental limit stress. A failure mode interaction, however, is likely and should be taken into account for future works.

With a calibrated, shear-modified Gurson model, a simulation of material fracture of SWRA was feasible and showed an overall good agreement with experimental data. A validation of the material modeling approach was reached with bolt-pull-out tests for complex stress states and fracture modes. Here, a crack arresting effect as well as a crack stimulating effect of the wires is visible. For the bolt-pull-out in wire direction, a ductile fracture mode of the matrix started, yet, the crack was stopped when reaching the wire. Subsequently, a shear crack ran along the wire, which supported the evolution of the crack. The bolt-pull-out perpendicular to wire direction encouraged the development of a crack within the aluminum matrix which led to an earlier fracture of the specimen.

From a modeling point of view, the discretization of the wires is crucial in many ways. With a coarse discretization, artificial interface forces are introduced. This does not allow for a decoupled numerical analysis of interface hoop shear and interface normal stress. In case of debonding, the created void is edged. This has a notch effect and may lead to premature fracture in the simulation.

It can be concluded, that debonding in SWRA is an important mode of material failure and must be considered. For pure tension in wire direction, the reinforcing effect of the introduced steel wires can be used, as the interface between matrix and wire keeps the wire from necking and postpones wire fracture up to high strains. For other load cases, arising interface normal stresses cause early debonding. This creates a void in the matrix which leads to premature fracture, so that a reinforcing effect of the steel wires cannot be fully exploited. If oriented disadvantageous, the wires can have a crack triggering effect and further support an evolution of the crack.

## Acknowledgement

The research presented in this paper was carried out within the Collaborative Research Centre SFB/Transregio10, subprojects A3 and C6, which are kindly supported by the German Research Foundation (DFG).

## References

[1] Hammers T, Weidenmann KA, Kerscher E. Mechanical properties of compound extruded aircraft stringer profiles under cyclic loading. Adv Engng Mat 2010;12(7):584–6.
[2] Wedekind M. Charakterisierung von Steifigkeit und Festigkeit heterogen verstärkter Verbundstrangpressprofile, Dissertation. München: TU München; 2013.
[3] Weidenmann KA, Schwind Th, Kerscher E, Löhe D. Cyclic loading of wire-reinforced aluminium matrix composite extrusions. Materialwiss Werkstofftech 2007;38(2):75–8.
[4] Kelly A, Davies GJ. The principles of the fibre reinforcement of metals. Metall Rev 1965;10(37):1–78.
[5] Weidenmann KA, Kerscher E, Schulze V, Löhe D. Mechanical properties of compound-extruded aluminium-matrix profiles under quasi-static loading conditions. Adv Mater Res 2006;10:23–4.
[6] Morasch A, Wedekind M, Matias D, Baier H. Thermo-mechanical behavior and material failure of steel wire reinforced aluminum. Proc CIRP 2014;18:144–9.
[7] Merzkirch M, Meissner M, Schulze V, Weidenmann KA. Tensile behaviour of spring steel wire reinforced EN AW-6082. Int J Compos Mater 2014;0:1–14.
[8] Zäh MF, Tekkaya AE, Langhorst M, Ruhstorfer M, Schober A, Pietzka D. Experimental and numerical investigation of the process chain from composite extrusion to friction stir welding regarding the residual stresses in composite extruded profiles. Prod Engng Res Devel 2009;3:353–60.
[9] Merzkirch M. Verformungs- und Schädigungsverhalten der verbundstranggepressten, federstahldrahtverstärkten Aluminiumlegierung EN AW-6082. Dissertation, Karlsruher Institut für Technologie, Schriftenreihe des Instituts für angewandte Materialien 2012;11.
[10] Weidenmann KA. Werkstoffsysteme für verbundstranggepresste Aluminiummatrixverbunde, Dissertation, Universität Karlsruhe, Karlsruhe; 2006.
[11] Merzkirch M, Reeb A, Weidenmann KA, Wanner A, Schulze V. Acoustic emission response of reinforced lightweight metal matrix composites during tensile and cyclic loading. Int J Acoust Emission 2011;29:317–28.
[12] Nahshon K, Huchinson JW. Modification of the Gurson Model for shear failure. Eur J Mech A Solid 2008;27:1–17.
[13] DIN 29 850. Luft- und Raumfahrt – Wärmebehandlung von Aluminium-Knetlegierungen; October 1989.
[14] DIN EN ISO 6892–1. Metallic materials – Tensile testing – Part 1: Method of test at room temperature (ISO 6892–1:2009); December 2009.
[15] Hockett JE, Sherby OD. Large strain deformation of polycrystalline metals at low homologous temperatures. J Mech Phys Solids 1975;23:87–98.
[16] Hora P. Advanced constitutive models as precondition for an accurate FEM-simulation in forming applications. Ulm: LS-DYNA Anwenderforum; 2006.
[17] Pfaffinger T. Parameteridentifikatino von analytischen Fließkurvenmodellen bei hohen Dehnungen. Semester thesis. Institute of Lightweight Structures. Technische Universität München. TUM-MW65/1336-SA; 2013.
[18] Q. Yin, Verfestigungs- und Schädigungsverhalten von Blechwerkstoffen im ebenen Torsionsversuch, Dissertation. Dortmund: TU Dortmund; 2014.
[19] Voce E. A practical strain-hardening function. Metallurgia 1955;51:219–26.
[20] Gurson AL. Continuum theory of ductile rupture by void nucleation and growth: Part I – Yield criteria and flow rules for porous ductile media. Trans ASME J Engng Mater Technol 1977;99:2–15.
[21] Tvergaard V, Needleman A. Analysis of the cup-cone fracture in a round tensile bar. Acta Metall 1984;32(1):157–69.
[22] Livermore Software Technology Corporation (LSTC). LS-DYNA Theory Manual. Livermore; 2006.
[23] Zhang ZL. A sensitivity analysis of material parameters for the Gurson constitutive model. Fatigue Fract Engng Mater Struct 1996;19:561–70.
[24] Koplik J, Needleman A. Void growth and coalescence in porous plastic solids. Int J Solids Struct 1988;24(8):835–53.
[25] Lemaitre J. Handbook of materials behavior models. San Diego: Acad. Press; 2001.
[26] Sun DT, Voss B, Schmitt W. Numerical prediction of ductile fracture resistance behavior based on micromechanical models. In: Defect Assessments in Components – Fundamentals and Applications. ESIS/EGF9. London: Mechanical Engineering Publications; 1991. p. 447–58.
[27] Zhang ZL, Hauge M. On the Gurson micro-mechanical parameters. Fatigue Fract Mech 1999;29:364–83.
[28] Peirs J, Verleysen P, Van Paepegem W, Degrieck J. Novel pure-shear sheet specimen geometry for dynamic material characterization. In: 9th International conference on the mechanical and physical behaviour of materials under dynamic loadings – DYMAT. Brussels, Belgium; 2009. p. 35–41.
[29] Marshall DB. An indentation method for measuring matrix-fibre frictional stresses in ceramic composites. J Am Ceram Soc 1984;67:259–60.
[30] Weidenmann KA, Kerscher E, Schulze V, Löhe D. Characterization of the interfacial properties of compound-extruded lightweight profiles using the push-out-technique. Mater. Sci. Engng. A. 2006;424:205–11.
[31] Chandra N, Ananth CR. Analysis of interfacial behavior in MMCs and IMCs by the use of thin-slice push-out tests. Comp Sci Technol 1995;54:87–100.
[32] Livermore Software Technology Corporation (LSTC). LS-DYNA Keyword Users Manual. vol. 2. Material Models, Version 971 R6.0.0. Livermore; 2012.
[33] Bhushan B, Ghupta BK. Handbook of Tribology – Materials, coatings, and surface treatments. New York: McGraw-Hill Inc.; 1991.
[34] Barlat F, Lege DJ, Brem JC. A six-component yield function for anisotropic materials. Int J Plast 1991;7:693–712.
[35] Schmeing F, Feucht M, Haufe A. Forming and crash induced damage evolution and failure prediction – Part I: Extension of the Gurson model to forming simulations. In: 6. LS-DYNA. Frankenthal: Anwenderforum; 2007. p. H-I-1–H-I-10.